Unfolding reaction mechanisms in ^{12}C fusion with Zr below 7 MeV/nucleon

Malvika Sagwal and Moumita Maiti[*]

Department of Physics, Indian Institute of Technology Roorkee, Roorkee-247667, Uttarakhand, India

Heavy-ion reaction studies in the incident energy regime $\leqslant 20$ MeV/nucleon have suggested multiple signatures of preequilibrium emission during the compound nucleus formation phenomenon and the presence of incomplete fusion, both of which vary with the incident energy and projectile-target combination. However, the available reaction data are insufficient to accurately decipher these contributions as the reports have a finite dependency on the predictions from theoretical models. Therefore, sound data interpretation with robust nuclear models is fundamental to unfolding the underlying processes. We report a new study of excitation functions of residues produced from the ^{12}C +Zr reactions up to 6.3 MeV/nucleon energy. Cross sections of 16 evaporation residues were measured through off-beam γ-ray spectroscopy. Excitation functions of the evaporation residues are reported at 14 energy points and compared with the reaction model code EMPIRE-3.2.2, with variations in nuclear level density. Additionally, the overall contribution of precompound and compound nuclear processes is discussed quantitatively within the realms of EMPIRE-3.2.2 model code.

I. INTRODUCTION

The dynamics of heavy-ion (projectile mass > 4) interactions continue to attract significant research interest due to the richness of the reaction phenomena. These phenomena broadly span direct, fusion, fusion-fission, and quasifission reactions depending on the projectile angular momentum and energy. The compound nuclear reaction is mostly observed after fusion in the low energy regime ($\leqslant 20$ MeV/nucleon). Bohr's independence hypothesis considers that the compound nucleus equilibrated in all degrees of freedom, such as mass and energy, forgets its memory of formation, and de-excites through isotropic emission of light particles, clusters, and γ rays. During the evolution process, the composite system with high excitation energy (E^*) often emits pre-equilibrated (PEQ) light-fast particles (LFPs), p, n, α-particle, etc. The LFPs are primarily emitted in the forward direction and are the principal signatures of the PEQ process. These particles supply valuable information about the dynamics of an excited composite system and the subsequent mechanism by which it achieves statistical equilibrium.

The PEQ phenomena have been witnessed for energies $\geqslant 10$ MeV/nucleon [1–5] as well as <10 MeV/nucleon [6–21] so far. Although several methods have been tried to study PEQ emission, the analysis of excitation functions (EFs) from the light and heavy-ion induced reactions deserves specific attention as their trend at low, moderate, and high energies can explicitly reveal the signature of reaction mechanisms involved. A unique signature of the PEQ process has been observed in the high-energy tail of the EFs for specific evaporation channels [14]. Because the inference of

the reaction mechanism is highly dependent upon the theoretical models, models carrying a more robust and holistic approach to the reaction phenomena are desired. Choosing the best systematic framework continues to be an active research area. The combination of Hauser-Feshbach [22] and Griffin's exciton model [23] has turned out to be a versatile choice for explaining the EQ (equilibrium) and PEQ processes, respectively, for heavy-ion reactions. The aforementioned models have satisfactorily explained the ^{6,7}Li, ^{11}B, and ^{12}C-induced reaction data below 7 MeV/nucleon energy [10–14].

The analyses of heavy-ion reaction data over a wide range of projectiles have suggested that, in addition to complete fusion (CF), contributions from breakup fusion or incomplete fusion (ICF), deep-inelastic collisions, and other nonfusion processes start competing at relatively high incident energies ($\geqslant 10$ MeV/nucleon). The onset of the ICF phenomenon is lately discussed for energies even below 10 MeV/nucleon [15–21,24–28]. In this regard, the cluster-structured beams, which are prone to breakup, carry significant importance in studying many reaction processes during the heavy-ion interaction [6,7].

^{12}C is an interesting projectile because of its α-clustered structure and the Hoyle state at 7.65 MeV, just above its 3α breakup threshold of 7.27 MeV. Although it has a finite probability of breakup into fragments, ^{8}Be +α, ^{12}C is considered a strongly bound projectile with α-separation energy ($E_\alpha = 7.37$ MeV) higher compared to other weakly bound stable projectiles, e.g., ^{6,7}Li and ^{9}Be with $E_\alpha = 1.47$, 2.47, and 2.46 MeV, respectively. Additionally, some medium mass targets (^{89}Y, ^{nat}Zr, ^{93}Nb, and ^{nat}Mo) [15–19] have shown considerable ICF contribution along with CF for weakly bound ^{6,7}Li projectiles, while the same was not observed for ^{12}C + ^{89}Y and ^{93}Nb [10,11] below 7 MeV/nucleon incident energy. It seems likely that the suppression in the CF is sensitive

towards the projectile's E_α as noticed by Rath *et al.* also [28]. The theory by Morgenstern *et al.* [29] emphasizes that, for a fixed value of $v_{rel} = [2(E_{c.m.} - V_B)/\mu]^{1/2}$, the strength of ICF should increase with mass asymmetry in the incoming channel. The same was established [10,30] through ^{12}C-induced EF measurement conducted with a variety of targets, from the medium to the heavy mass region, such as ^{93}Nb, ^{103}Rh, ^{115}In, ^{128}Te, ^{159}Tb, ^{165}Ho, ^{181}Ta [5,10,30–35]. Significant PEQ emissions during the CF and ICF processes were also observed in ^{12}C + ^{64}Ni, ^{93}Nb, ^{181}Ta, and ^{197}Au [6,8–10]. The choice of model codes plays a crucial role in understanding the reaction mechanism and quantifying the contribution of different processes.

Despite constant efforts, the plethora of interplay between the CF-ICF and EQ-PEQ processes for ^{12}C-induced reactions brings interesting aspects of heavy-ion fusion dynamics that need to be systematically understood. It prompted us to present the first understanding of the ^{12}C + Zr reaction below 7 MeV/nucleon through an evaporation residue (ER) measurement study. The EMPIRE-3.2.2 model code was used to infer the reaction mechanism. Though it is a new study, our understanding has benefited from the previous nuclear reaction studies carried out in this mass region. The experimental part and the nuclear model code used are explained in Secs. II and III, respectively. In Sec. IV and V, we discuss the results and conclude the report.

II. EXPERIMENTAL PROCEDURE

A. Details of experimental setup

The experiment was performed at the 14 UD BARC-TIFR Pelletron facility in Mumbai, India. Self-supporting targets of spectroscopically pure natural Zr prepared through the rolling technique were used. Zr foils (1.4–3 mg/cm^2) stacked alternatively with the ^{27}Al catcher foils (1.6–1.8 mg/cm^2) were placed in front of the ^{12}C beam. The maximum energy of the beam was 77 MeV while the charge state was kept between 5$^+$ and 6$^+$. Al-catcher foils were placed for trapping the recoiling ERs and for energy degradation to achieve a wide range of energy points. Five stacks consisting of 2–3 target-catcher assemblies were irradiated with different energies for 2.5–5 h with an average beam current of 470 μC, in a way that some overlapping energy points could be obtained. A Faraday cup was put behind the target chamber to measure the total dose or charge dissipated by the beam during irradiation. The energy degradation inside each target was calculated through Stopping and Range of Ions in Matter (SRIM) software [36]. The energy (E) considered inside each target for analysis was the average of the incident and outgoing energies. Fourteen energy points ranging from 40.2 to 76.2 MeV (laboratory frame) were achieved that were higher than the reaction Coulomb barrier (maximum 37.1 MeV for ^{12}C + ^{90}Zr). Irradiation was carried out by keeping the half-life ($T_{1/2}$) of residues in mind as well as possible errors in the activity due to large irradiation time.

B. Measurement of activity

Post irradiation, each target-catcher foil was assayed using a precalibrated high purity germanium (HPGe) detector by ac-

quiring the γ-ray spectrum of the radionuclides formed at that energy. The detector was calibrated with the standard sources of known activities, namely ^{152}Eu (13.517 yr) and ^{60}Co (5.27 yr). The energy resolution of the HPGe was 2 keV for the 1332 keV γ-ray peak. The γ-ray spectrum was obtained by multichannel analyzer coupled to a system operating with GENIE-2k (Canberra) software. Each reaction product was identified through the characteristic γ rays and decay profile, which confirms its $T_{1/2}$. Background subtracted area counts under a particular energy peak were used to estimate the yield or activity of the residues at the end of bombardment (EOB) following the given method in Ref. [37]:

$$Y^r = \frac{C(t)}{\varepsilon_\gamma I_\gamma^r} e^{\lambda^r T_w},$$ (1)

where Y^r is the yield of residue r, and $C(t)$ is the count rate (count per second) at time t. ε_γ and I_γ^r are the geometry-dependent detection efficiency of HPGe and branching intensity of the characteristic γ-ray of the residue. λ^r is the decay constant of the residue, and T_w is the waiting/cooling time. Thereafter, the production cross section of the residue r at energy E can be calculated through the activation formula:

$$\sigma^r(E) = \frac{\lambda^r Y^r T_c}{I_{beam} N_{tg}(1 - e^{-\lambda^r T_i})(1 - e^{-\lambda^r T_c})}.$$ (2)

I_{beam} is the intensity of the projectile ions, and N_{tg} is the areal density of the target (number of target nuclei per unit area). T_i and T_c are the duration of irradiation and counting, respectively. The nuclear spectroscopic data used to calculate the cross section are listed in Table I. We preferred to estimate the cross section from as many confirmed γ rays as possible. However, for some residues, only one γ ray peak was considered, either due to the absence of other intense γ rays peaks or due to the limitations of measurement (merging with nearby γ rays, poor counting statistics, etc.). Nevertheless, to maintain consistency in cross section estimation, its weighted average was calculated from individual cross sections obtained from different γ rays. The weighted averaged cross sections were used in further analysis and are also tabulated in Tables II and III.

C. Sources of error

Errors or uncertainties might have crept into the measurement from the following sources:

(i) Variation up to 2% in the geometry-dependent efficiency of the detector. The γ-ray's energy value also plays an important role here.

(ii) Uncertainty of a maximum of 7% was considered in the measurement of the beam flux due to fluctuation in beam current.

(iii) Inaccuracy in the measurement of target thickness and nonuniformity of the target was also taken into account, and a total error of 2% was considered.

(iv) Error exists in the area counts due to counting statistics as well as the strength of the γ ray under consideration.

TABLE I. Spectroscopic data [38] of the radionuclides along with their contributing processes.

Nuclide (J^π)	$T_{1/2}$	Decay mode (%)	E_γ (keV) [I_γ (%)]	Contributing reactions
^{101}Pd[a] (5/2$^+$)	8.47 h	ϵ[b] (100)	296.29 [19], 269.67 [6.43] 565.98 [3.44], 1289.04 [2.28]	^{nat}Zr (^{12}C, xn)
^{100}Pd (0$^+$)	3.63 d	ϵ (100)	84.00 [52], 74.78 [48] 126.15 [7.8]	^{nat}Zr (^{12}C, xn)
^{99}Pd (5/2$^+$)	21.4 min	ϵ (100)	136.0 [73], 1335.6 [4.7] 399.8 [3.6], 786.6 [3.4]	^{nat}Zr (^{12}C, xn)
^{98}Pd (0$^+$)	17.7 min	ϵ (100)	112.2 [57.9], 106.8 [13.7]	^{nat}Zr (^{12}C, xn)
^{101m}Rh (9/2$^+$)	4.34 d	IT[c] (7.20), ϵ (92.80)	306.857 [81]	^{nat}Zr (^{12}C, pxn) + ^{101}Pd (ϵ)
^{100}Rh (1$^-$)	20.5 h	ϵ (100)	539.512 [80.6], 822.654 [21.09] 1553.348 [20.67], 1362.152 [15.39] 1107.223 [13.57], 446.153 [11.98]	^{nat}Zr (^{12}C, pxn)
^{99m}Rh (9/2$^+$)	4.7 h	IT (< 0.16%), ϵ (> 99%)	340.8 [72], 617.8 [12.3] 1261.2 [11.4], 276.6 [1.67]	^{nat}Zr (^{12}C, pxn) + ^{99}Pd (ϵ)
^{97g}Rh (9/2$^+$)	30.7 min	ϵ (100)	421.55 [74.63], 840.13 [12] 878.8 [9]	^{nat}Zr (^{12}C, pxn)
^{97m}Rh (1/2$^-$)	46.2 min	IT (5.6), ϵ (94.4)	189.21 [48.5]	^{nat}Zr (^{12}C, pxn)
^{97}Ru (5/2$^+$)	2.83 d	ϵ (100)	215.70 [85.62], 324.49 [10.79]	^{nat}Zr (^{12}C, αxn) + ^{97}Rh (ϵ)
^{95}Ru (5/2$^+$)	1.643 h	ϵ (100)	1096.8 [20.9], 626.83 [17.8] 1178.7 [5.13], 806.28 [4.04] 290.38 [3.68]	^{nat}Zr (^{12}C, αxn)
^{94}Ru (0$^+$)	51.8 min	ϵ (100)	367.2 [75]	^{nat}Zr (^{12}C, αxn)
^{96}Tc (7$^+$)	4.28 d	ϵ (100)	778.22 [99.76], 849.86 [98.0] 812.54 [82.0], 1126.85 [15.2]	^{nat}Zr (^{12}C, αpxn)
^{95}Tc (9/2$^+$)	20.0 h	ϵ (100)	765.789 [93.8], 1073.71 [3.74] 947.67 [1.952]	^{nat}Zr (^{12}C, αpxn) + ^{95}Ru (ϵ)
^{94}Tc (7$^+$)	293 min	ϵ (100)	871.05 [99.9], 702.67 [99.6]	^{nat}Zr (^{12}C, αpxn) + ^{94}Ru (ϵ)
^{93m}Mo (21/2$^+$)	6.85 h	IT (99.88), ϵ (0.12)	684.693 [99.9], 1477.138 [99.1] 263.049 [57.4]	^{nat}Zr (^{12}C, $2\alpha xn$)
^{89}Zr (9/2$^+$)	78.41 h	ϵ (100)	909.15 [99.04]	^{nat}Zr (^{12}C, $3\alpha xn$)

[a]Decay radiation information not found in Ref. [38] was taken from Ref. [39].
[b]Electron capture.
[c]Isomeric transition.

(v) Dead time of the detector was kept small by adjusting the geometry of measurement.

Error in cross section measurement was estimated and, on average, was found to be ≈ 15% taking all the factors into account. Additionally, we have critically examined the variability of cross sections attained from different γ rays, but the weighted average was considered to mitigate the differences, howsoever small. However, a few residues, e.g.,

TABLE II. Measured cross section (mb) of residues at different incident energies

E_{lab} (MeV)	^{101}Pd	^{100}Pd	^{99}Pd	^{98}Pd	^{101m}Rh	^{100}Rh	^{99m}Rh[a]	$^{97g+m}$Rh
40.2 ± 1.4	13.7 ± 2.7				7.9 ± 2.2		3.8 ± 1.3	
41.4 ± 2.9	37.1 ± 5.1	40.8 ± 5.2	9.8 ± 1.7		15.8 ± 2.6	34.8 ± 4.2	32.8 ± 4.0	
46.5 ± 1.3	52.1 ± 7.8	48.9 ± 6.6	42.8 ± 10.8		28.8 ± 6.0	41.3 ± 6.3	88.8 ± 10.9	
50.0 ± 2.6	88.8 ± 11.1	51.2 ± 6.1	90.9 ± 16.1		45.7 ± 6.4	58.1 ± 6.9	260.9 ± 29.9	
53.5 ± 2.5	70.2 ± 9.6	43.7 ± 6.0	94.2 ± 19.6		33.3 ± 5.6	43.5 ± 5.8	256.0 ± 28.0	
55.6 ± 1.2	68.3 ± 9.6	49.2 ± 5.7	116.7 ± 15.5	4.3 ± 1.0	46.5 ± 5.5	55.9 ± 6.5	329.0 ± 33.4	
57.8 ± 2.4	54.8 ± 7.6	60.8 ± 9.0	82.3 ± 25.0	5.2 ± 1.0	34.4 ± 5.1	46.9 ± 5.8	275.4 ± 27.2	
60.8 ± 1.1	40.2 ± 5.6	50.5 ± 6.4	77.4 ± 11.8	12.0 ± 2.0	26.8 ± 3.5	48.5 ± 5.7	240.4 ± 27.0	
61.0 ± 2.3	35.8 ± 5.3	62.3 ± 9.5	64.7 ± 13.9	8.3 ± 1.0	26.3 ± 4.4	44.5 ± 6.0	240.5 ± 27.2	
65.0 ± 2.3	45.6 ± 6.6	50.5 ± 6.7	52.5 ± 9.5	14.1 ± 2.2	34.2 ± 4.9	63.6 ± 8.2	282.2 ± 30.1	1.6 ± 0.4
66.2 ± 1.1	45.3 ± 6.5	44.8 ± 5.5	61.3 ± 9.0	21.8 ± 3.4	32.5 ± 4.5	63.5 ± 7.6	223.1 ± 25.6	4.8 ± 0.9
71.3 ± 1.0	49.9 ± 7.8	37.7 ± 4.8	39.5 ± 5.3	19.1 ± 3.2	36.3 ± 5.1	52.8 ± 6.6	165.6 ± 20.7	25.0 ± 8.7
71.7 ± 2.1	60.5 ± 8.4	44.0 ± 5.8	35.5 ± 5.1	20.6 ± 4.0	49.0 ± 5.6	72.5 ± 8.6	228.1 ± 26.3	25.5 ± 2.9
76.2 ± 1.0	60.9 ± 9.3	27.6 ± 3.7	36.2 ± 6.0	19.5 ± 2.9	53.1 ± 6.8	50.6 ± 6.5	158.2 ± 21.6	71.3 ± 7.2

[a]Cumulative production cross section.

TABLE III. Measured cross section (mb) of residues at different incident energies

E_{lab} (MeV)	^{97}Ru[a]	^{95}Ru	^{94}Ru	^{96}Tc	^{95}Tc[a]	^{94}Tc[a]	^{93m}Mo	^{89}Zr
40.2 ± 1.4	3.3 ± 0.7							
41.4 ± 2.9	17.7 ± 2.2							
46.5 ± 1.3	27.3 ± 3.6							
50.0 ± 2.6	46.7 ± 4.6							
53.5 ± 2.5	39.1 ± 4.6			7.2 ± 1.1	0.9 ± 0.2		1.2 ± 0.2	
55.6 ± 1.2	45.1 ± 5.2			13.0 ± 1.9	3.6 ± 0.6		3.6 ± 0.6	2.5 ± 0.5
57.8 ± 2.4	41.6 ± 4.7			17.7 ± 2.1	6.7 ± 0.8		4.3 ± 0.6	2.3 ± 0.4
60.8 ± 1.1	38.6 ± 4.5	8.9 ± 1.5		16.9 ± 2.2	20.1 ± 3.3		6.2 ± 0.9	2.9 ± 0.5
61.0 ± 2.3	39.6 ± 4.7	9.1 ± 1.4		18.8 ± 2.3	20.9 ± 2.2		6.2 ± 0.8	3.8 ± 0.7
65.0 ± 2.3	63.6 ± 6.9	22.0 ± 3.3		29.3 ± 3.3	55.7 ± 7.4	0.4 ± 0.1	12.3 ± 1.5	6.2 ± 0.9
66.2 ± 1.1	64.1 ± 7.2	25.1 ± 4.0		27.3 ± 3.4	68.9 ± 9.7	0.7 ± 0.1	13.4 ± 1.6	7.3 ± 1.1
71.3 ± 1.0	94.9 ± 10.3	41.0 ± 5.4	1.0 ± 0.2	26.5 ± 3.3	114.4 ± 14.0	4.3 ± 0.6	18.7 ± 2.1	9.7 ± 1.3
71.7 ± 2.1	154.3 ± 15.9	55.9 ± 7.9	1.4 ± 0.3	40.1 ± 4.5	168.4 ± 18.8	6.5 ± 0.8	25.4 ± 2.9	14.3 ± 1.6
76.2 ± 1.0	180.6 ± 19.1	62.1 ± 8.0	6.3 ± 0.7	32.0 ± 3.8	175.8 ± 21.8	20.5 ± 2.5	25.8 ± 3.0	16.3 ± 2.0

[a]Cumulative production cross section.

^{101m}Rh, ^{97m}Rh, ^{94}Ru, and ^{89}Zr, could be identified through only one characteristic γ ray peak for each. In the absence of other unidentified γ rays, an additional uncertainty of $<$ 5% is likely in reporting their cross sections. The error in energy estimation in targets has occurred due to inaccuracy in target thickness measurement. Second, the energy changes continuously throughout the target, but the average energy value was considered for analysis. Possible error caused due to change in the rate of energy degradation throughout the target was also considered for the energy error calculation. However, the straggling effect was considered insignificant.

III. COMPUTATION CODE: EMPIRE-3.2.2

The nuclear reaction model code EMPIRE-3.2.2 [40] extensively covers all the broad nuclear reaction areas, i.e., direct (DIR), PEQ, and EQ processes. In the case of DIR, the optical model is used for the calculation of transmission coefficients (T_ℓ) for all the outgoing nuclei. According to the target structure and inelastic excitations, the code can initiate the distorted wave Born approximation (DWBA) and simplified coupled-channels approach via the code CCFUS. EMPIRE can incorporate quantum-mechanical models [multistep direct (MSD) and multistep compound (MSC)], and classical phenomenological models (exciton model and hybrid Monte Carlo simulations, DDHMS) to account for the emission of PEQ γ-rays, particles, and clusters from the composite nucleus. The incident flux forming the composite system first undergoes the PEQ mechanism that forms the residual nuclei continuum, which further encounters full-fledged Hauser-Feshbach (HF) calculations [22] for the compound nuclear deexcitation process.

In the exciton model [23], the projectile enters the target energy continuum and forms excitons (particle-hole pairs). The number of excitons (n_0) tends to increase as there are more ways to redistribute excitation energy (E^*) among different levels. During this process, one or more nucleons might emit out of the continuum contributing to the PEQ emission process. The emission rate of nucleons is calculated from the Kalbach method [41], whereas an α-particle's

emission probability is calculated through Iwamoto-Harada model [42] parametrization. The Fermi-gas model (FGM) with backshifted pairing is used for level density calculation, as expressed below:

$$\rho^{FG}(E_x) = \frac{(2J+1)}{48\sqrt{2}\sigma^{3/2}a^{1/4}U^{5/4}} \exp\left[2\sqrt{aU} - \frac{(J+1/2)^2}{2\sigma^2}\right], \quad (3)$$

where J is the spin of intrinsic levels, and a is the level density parameter. $U = E_x - \Delta$ is the effective excitation energy where excitation energy $E_x = aT^2$ and Δ is equal to or closely related to the pairing energy. σ^2 is the spin cutoff parameter.

EMPIRE comprises three phenomenological level-density models, e.g., the Gilbert-Cameron model (GCM), the generalized superfluid model (GSM), and the enhanced generalized superfluid model (EGSM). GCM approach follows the constant temperature formula at low E_x below matching point U_x and the FGM formula above U_x. GSM incorporates a phase transition from superfluid behavior to FGM at critical temperature T_c. EGSM's systematics are mostly similar to GSM's, but it allows more accurate treatment of angular momenta through spin distribution in FGM. So its utility is naturally better for heavy-ion reaction study.

In the present calculations, the HF model and exciton model PCROSS with mean free path parameter 1.5 were chosen. The DWBA calculation for all the collective levels was also incorporated using the generic parameters of EMPIRE. Other relevant information, such as optical model parameters, nuclear masses, ground-state deformations, Kalbach systematics, angular distributions, level densities, γ-ray strength functions, fission barriers, etc., were taken from the input library database RIPL-3 [43].

IV. RESULTS AND DISCUSSION

The ^{12}C + ^{nat}Zr reaction was carried in the range 40.2–76.2 MeV or 3.4–6.3 MeV/nucleon, whereas the maximum coulomb barrier was 37.1 MeV. The compound and precompound reaction processes are expected in this energy range. As far as the compound nuclear part is concerned, the interaction
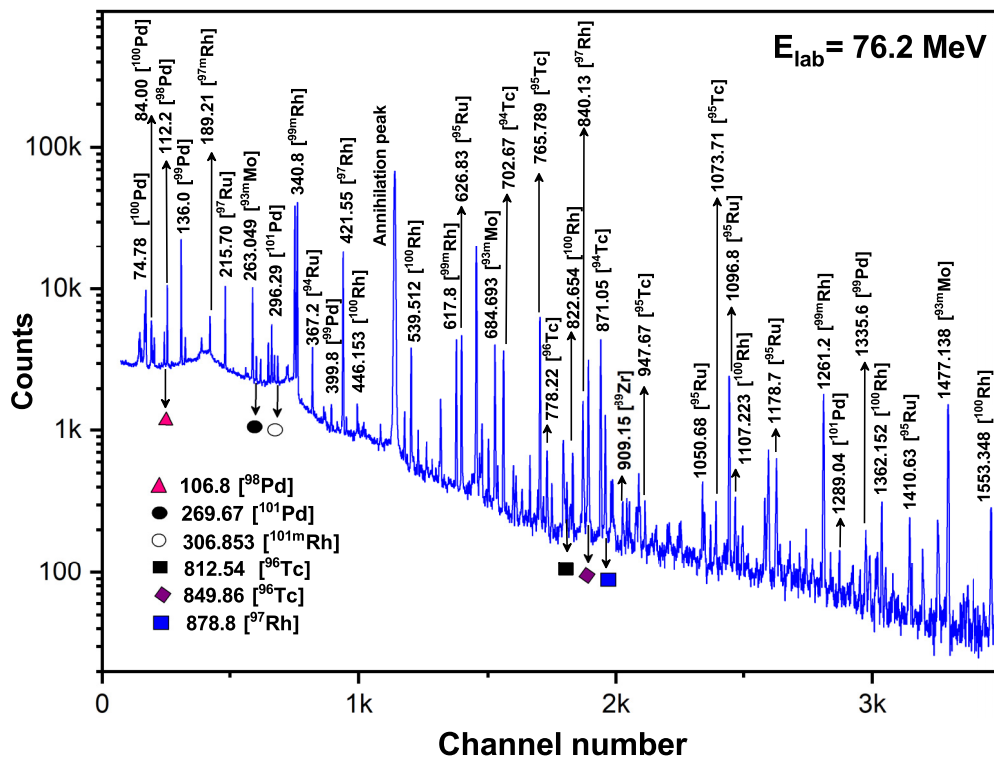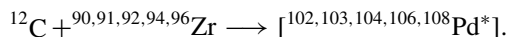
FIG. 1. γ ray profile of the 76.2 ± 1.0 MeV ^{12}C irradiated Zr target obtained 25.8 min after the end of bombardment (EOB). The energies of γ-rays are in keV.

can result in the following compound nuclei through CF:

$$^{12}\text{C} + {}^{90,91,92,94,96}\text{Zr} \longrightarrow [{}^{102,103,104,106,108}\text{Pd}^*].$$

The excitation energy (E^*) of the equilibrated compound nucleus is 35.8–67.6 MeV. The isotropic emission of light particles leaves behind evaporation residues (ERs), which might be stable nuclei or unstable radionuclides emitting γ rays. The time-resolved γ-ray spectrum obtained 25.8 min after the EOB for 76.2 MeV irradiation is shown in Fig. 1, where the characteristic peaks are marked with corresponding decaying radionuclides. The radionuclides, viz., ^{101,100,99,98}Pd, ^{101m,100,99m,97}Rh, ^{97,95,94}Ru, ^{96,95,94}Tc, ^{93m}Mo, and ^{89}Zr, were identified in the reaction. For further confirmation, $T_{1/2}$ were extracted from their decay profiles (Fig. 2) and compared with those available in the database NuDat 3.0 [38]. The cross sections were estimated (Sec. II B) and are listed in Tables II and III. In order to understand the reaction mechanism, data were compared with EMPIRE-3.2.2 with different level densities (Sec. III).

A. Excitation function analysis

1. xn channels

The excitation functions (EFs) of ^{101,100,99,98}Pd populated via *xn* channel from the excited compound nucleus were plotted (Fig. 3). For ^{101}Pd, EMPIRE with EGSM level density is in good agreement with the experimental data throughout the energy range [Fig. 3(a)]. However, GSM and GCM explain the measured cross sections (σ) only partially. While the former
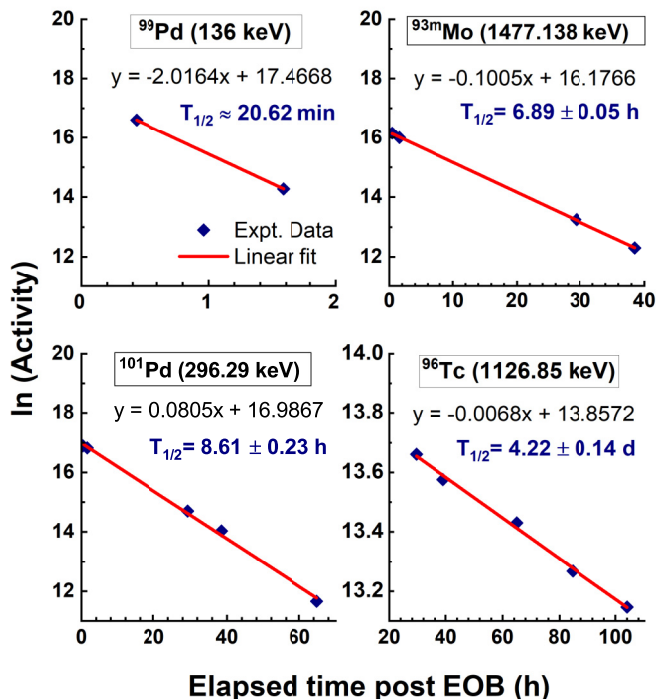

FIG. 2. Activity profiles of a few residues obtained as a function of elapsed time after the end of bombardment (EOB). In other words, it is the time difference between the stop of irradiation and start of γ-ray acquisition. The extracted half-lives ($T_{1/2}$) of the residues range from minutes to days.
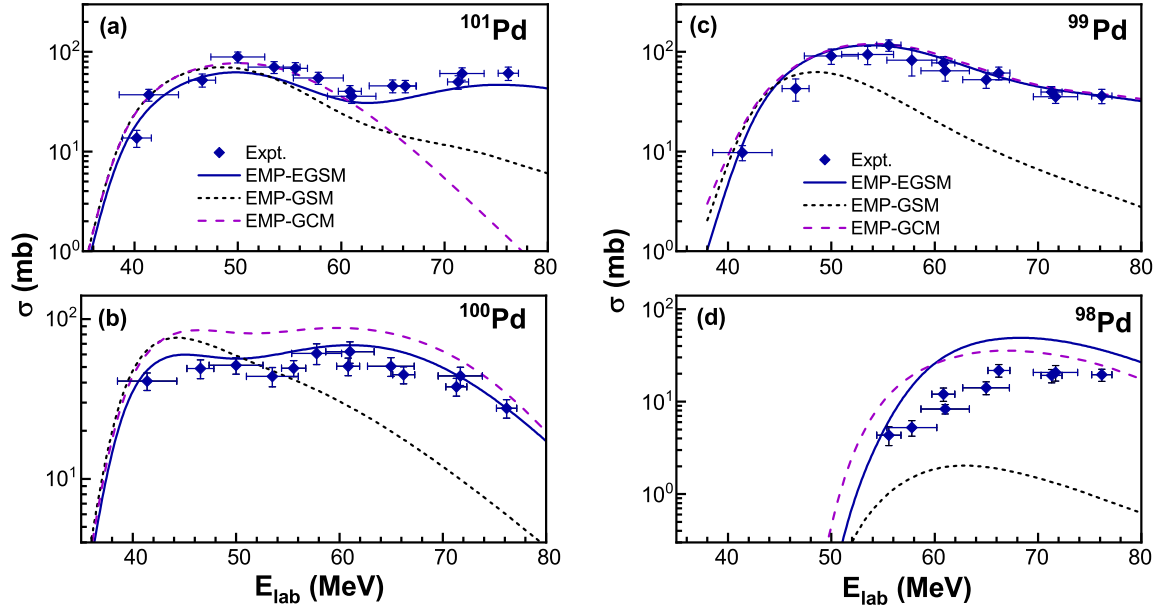
FIG. 3. Comparison of experimental (solid diamonds) excitation functions of Pd residues produced by the *xn* channel with those obtained from theoretical estimation from EMPIRE-3.2.2 (solid/dashed lines).

explains the data nearly up to 48 MeV and goes downwards after that, the latter keeps following the data very well up to 60 MeV and descends sharply at higher energies. The EFs of ^{100,99}Pd are again justified satisfactorily by EMPIRE-EGSM for the former; and EGSM and GCM for the latter [Figs. 3(b) and 3(c)]. From the onset of disagreement with GSM at lower energies, the trend continues throughout the EF. For ^{98}Pd, none of the level densities of EMPIRE are entirely able to justify the trend [Fig. 3(d)].

Overall, EMPIRE-EGSM shows a good level of data prediction for the *xn* channel. The disagreement among different EMPIRE level densities should be due to their underlying difference in constant temperature approach and superfluid behavior approach below U_x and T_c, respectively. Above all, EGSM embodies a better treatment for angular momenta and hence becomes the most accurate choice for heavy-ion reactions.

It should be added that each residue may form through several possible evaporation channels through ^{12}C$+^{90,91,92,94,96}$Zr reactions. ^{nat}Zr has isotopic abundance of ^{90}Zr 51.45%, ^{91}Zr 11.22%, ^{92}Zr 17.15%, ^{94}Zr 17.38%, and ^{96}Zr 2.8%. It poses an inherent challenge in finding the overall extent of PEQ emission. For instance, Fig. 4 shows that there might exist some cross section enhancement due to PEQ emission in ^{101}Pd towards the high energy tail through ^{12}C $+ ^{90,91,92}$Zr. However, it might get suppressed by ^{12}C $+ ^{94}$Zr in the equilibrium region where cross sections are relatively high. The same fact extends over all the populated ERs where the contributions from distinct reactions add up in different proportions.

2. pxn channels

Subsequently, the formation of Rh isotopes was observed through the *pxn* channel. The radionuclide ^{101m}Rh ($T_{1/2} =$ 4.34 d), along with its normal route of formation, was strongly

fed from electron capture (ϵ) decay of its higher charge precursor ^{101}Pd ($T_{1/2} = 8.47$ h). Figure 5 depicts the measured activity (Bq) of ^{101m}Rh against the elapsed time. One can see that, with the decay of ^{101}Pd, the production of ^{101m}Rh is increasing. However, after the passage of nearly $(4–5)T_{1/2}$ of ^{101}Pd, the cumulative count rate of ^{101m}Rh starts falling gradually. By this time, ^{101}Pd mostly vanishes and stops contributing. Nearly 4000 Bq of maximum contribution at 71.7 MeV was observed.

Figure 6(a) represents the EF of ind-^{101m}Rh (independent), where the measurements with only two hours of waiting time (T_w) after the EOB were considered to ensure the minimal
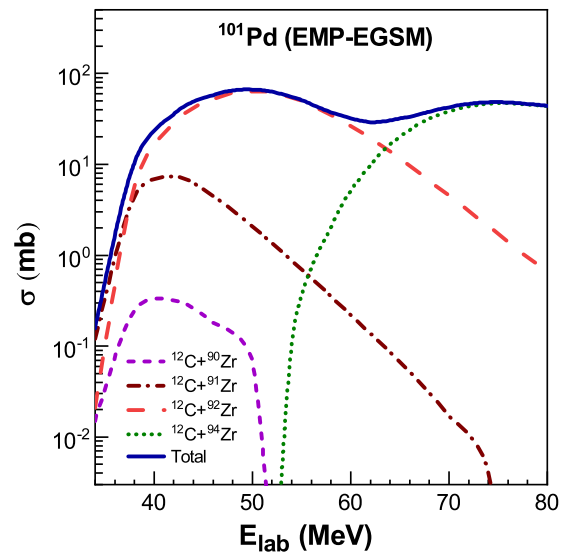

FIG. 4. EMPIRE-EGSM predicted excitation functions of ^{101}Pd from the ^{12}C $+ ^{nat}$Zr reaction. The contribution from different reactions is multiplied by the respective abundances of Zr isotopes.
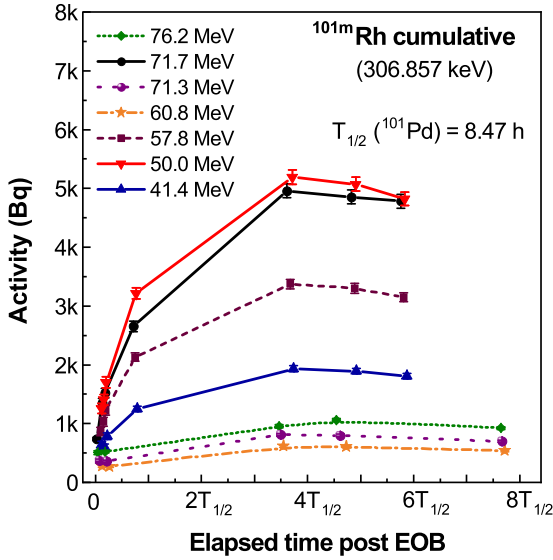
FIG. 5. Cumulative or measured activity of ^{101m}Rh for 306.857 keV γ-ray as a function of elapsed half-life ($T_{1/2}$) of ^{101}Pd after end of bombardment (EOB). The lines are guides to the eyes.

activity contribution from the decay of ^{101}Pd. It seems evident that EMPIRE-EGSM level density agrees better with the experimental data throughout the energy range. At the same time, GSM and GCM estimations overpredict and underpredict the data beyond 50 and 60 MeV, respectively.

Figure 6(b) (^{100}Rh) similarly shows that EMPIRE with EGSM level density is very well justifying the experimental data while GSM and GCM both overpredict the data beyond 46 MeV. Meanwhile, the long-lived precursor of ^{100}Rh (20.5 h), i.e., ^{100}Pd (3.63 d) decays through 100% ϵ. However, its

TABLE IV. Contribution to the production of residues through the decay of their parent radionuclides using Eq. (4).

Residue of interest	Parent's branching ratio P^p	Contribution of parent (mb)
^{99m}Rh	97.41% ϵ	$1.054 \times \sigma$ (^{99}Pd)
^{97}Ru	100% ϵ	$1.011 \times \sigma$ ($^{97g+m}$Rh)
^{95}Tc	100% ϵ	$1.090 \times \sigma$ (^{95}Ru)
^{94}Tc	100% ϵ	$1.215 \times \sigma$ (^{94}Ru)

contribution to the former is minimized by considering the activity data of a maximum 6 h of T_w post-EOB.

Cumulative production was also measured for ^{99m}Rh as ^{99}Pd (21.4 min) decays into the ground and isomeric state of ^{99}Rh with $T_{1/2} = 16.1$ d and 4.7 h, respectively. To extract the independent cross section of ^{99m}Rh, the following formalism by Cavinato *et al.* [6] was applied;

$$\sigma_d^{\text{ind}} = \sigma_d^{\text{cum}} - \sigma_p P^p \left[\frac{T_{1/2}^d}{T_{1/2}^d - T_{1/2}^p} \right] \qquad (4)$$

where σ_d^{ind} and σ_d^{cum} are the independent and cumulative production cross sections, respectively, of the daughter nucleus (^{99m}Rh). σ_p is the production cross section of the parent nucleus, ^{99}Pd. P^p stands for the branching ratio of parent to daughter nucleus, $T_{1/2}^d$ and $T_{1/2}^p$ are half-lives of daughter and parent nuclei, respectively. Following Eq. (4), the information on contribution is given in Table IV, while the cumulative or measured cross section of ^{99m}Rh is given in Table II. The maximum contribution of 123 mb is seen at 55.6 MeV. ^{99g}Rh has been neither observed nor significantly predicted by EMPIRE.
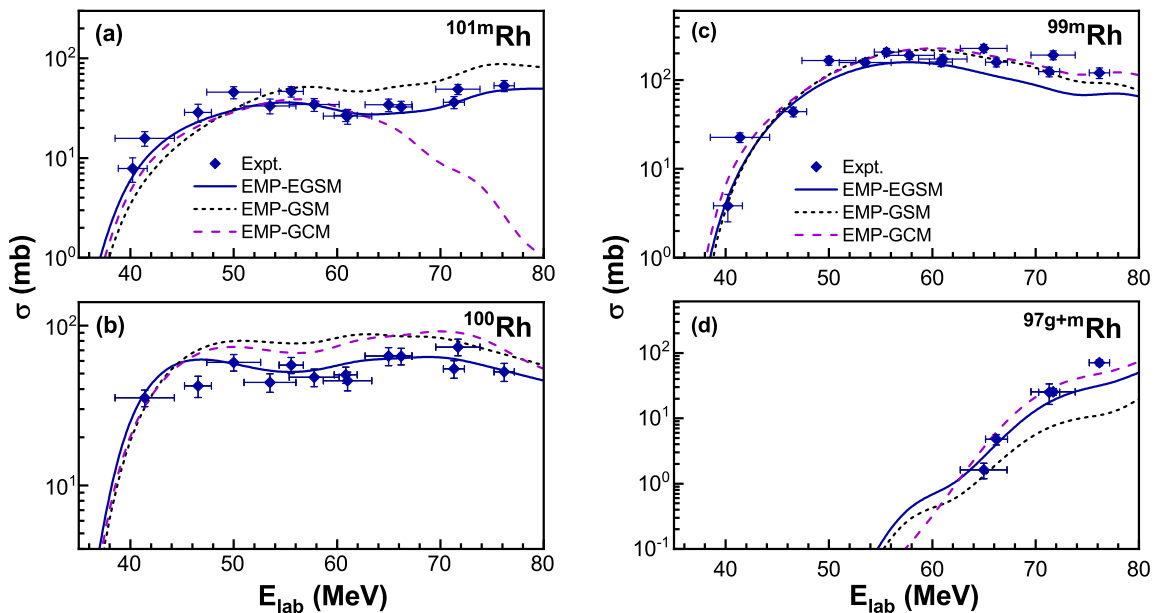

FIG. 6. Same as Fig. 3 for Rh residues obtained through the *pxn* channel. The extracted independent cross section for ^{99m}Rh has been plotted.
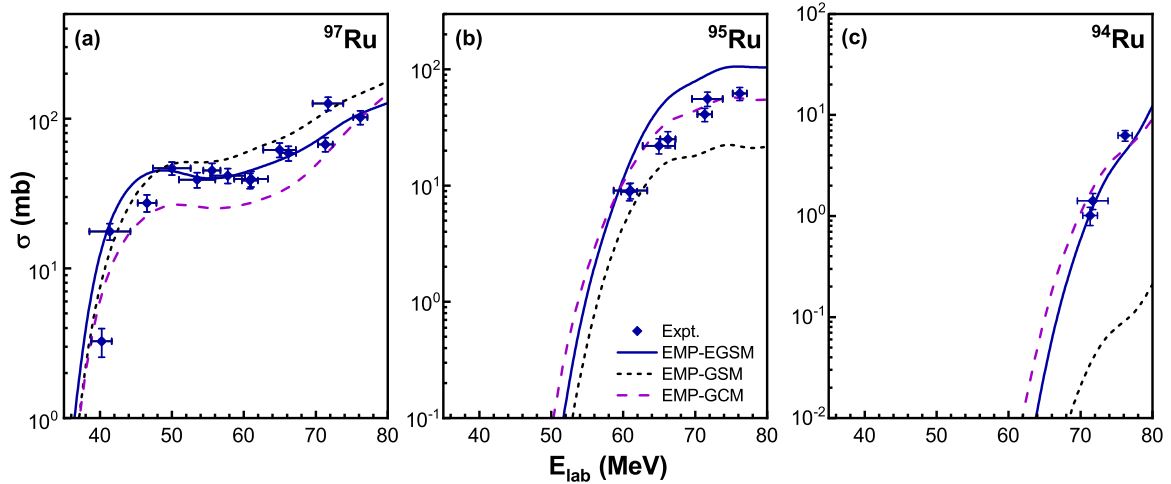
FIG. 7. Same as Fig. 3 for Ru residues obtained through the $\alpha x n$ channel. The extracted independent cross section for ^{97}Ru has been plotted.

From the EF of ind-^{99m}Rh, it is pretty clear that for energies up to ≈ 56 MeV, all the EMPIRE level densities hold a good fit with the experimental data, but at higher energies, only GSM and GCM justify the same [Fig. 6(c)]. In this reaction, ^{99m}Rh has the maximum independent production cross section with the highest value of 227 mb at 65 MeV.

Fig. 6(d) represents the EF of $^{97g+m}$Rh. ^{97m}Rh (46.2 min) decays to ^{97g}Rh (30.7 min) through 5.6% IT. Moreover, the $T_{1/2}$ of both is not very different, and it was challenging to segregate them through their decay radiations as both decay to ^{97}Ru with 94.4% and 100% ϵ, respectively. Therefore, the cross section of $^{97g+m}$Rh was compared with the theory. The trend insists that while different EMPIRE level densities follow the experimental trend in different energy ranges, GCM's predictions lie closest to the data on a reasonable level.

3. αxn and αpxn channels

Cumulative production was observed for ^{97}Ru (2.83 d) due to the decay of short-lived ^{97g,m}Rh. As ^{97}Ru was measured for more than four days, it effectively contains the full contribution ($P^p = 100\%$) from $^{97g+m}$Rh. A maximum of 78 mb contribution was found at 76.2 MeV.

Figure 7 depicts the EFs of ind-^{97}Ru and ^{95,94}Ru through the $\alpha x n$ or $2pxn$ channel. As the α particle requires a lower emission threshold and is also likely to form due to high excitation in the compound nucleus, its emission should be more favored. For ^{97}Ru, EMPIRE with EGSM and GSM explain the data at lower energies up to 50 MeV. However, at intermediate and higher energies, only EGSM fully justifies the data, while GSM and GCM closely follow the trend. For ^{95}Ru, EMPIRE-GCM fully explains the data. At the highest incident energy, GSM underpredicts the values by nearly 70%, while EGSM overpredicts them nearly twice. In the case of ^{94}Ru, EMPIRE-EGSM and GCM follow the data closely, where EGSM shows an overall better agreement.

Through the $\alpha p x n$ channel, Tc isotopes were produced. For ^{96}Tc [Fig. 8(a)], at higher energies, EMPIRE is not able to follow the trend, yet GCM level density prediction is in closer proximity to the experimental data.

Cumulative production was observed for ^{95,94}Tc (20.0 h, 293 min) as their parent radionuclides viz., ^{95,94}Ru (1.643 h, 51.8 min) are short-lived and decay through 100% ϵ (Table IV). After the lapse of nearly five $T_{1/2}$ (7 h) of ^{95}Ru, ^{95}Tc was measured with the addition of its parent's activity, which was subsequently removed. A maximum of 68 mb contribution was observed at 76.2 MeV. In the EF of ind-^{95}Tc, almost all the EMPIRE level densities exhibit a good agreement with the experimental data [Fig. 8(b)]. In the same line, a small activity contribution of ^{94}Ru was eliminated from ^{94}Tc. EMPIRE-GSM agrees well with the experimental data of ind-^{94}Tc, considering the error bar range for the lowest energy [Fig. 8(c)]. While EGSM consistently overpredicts the data, GCM only agrees with the data at lower energies.

4. 2αxn and 3αxn channels

^{93m}Mo and ^{89}Zr were emitted via $2\alpha x n$ and $3\alpha x n$ channels, respectively (Fig. 9). From the fusion of two α particles in the composite system, ^{8}Be can also form and emit; however, the statistical chances of its formation are very low. From the EF of ^{93m}Mo, only partial justification of the EF can be inferred from different EMPIRE level densities. For ^{89}Zr, a sizable relative enhancement in cross section with respect to theory might be due to the contribution from ICF or a massive transfer process, which the model code does not considere. Some ^{12}C flux might have broken up into ^{8}Be $+\alpha$, and α has most likely fused with the target to form a Mo* compound nucleus. It might have resulted in ERs, viz., ^{93m}Mo and ^{89}Zr, with the contribution of ICF being more evident for the latter. Though very small, the measured difference or the ICF cross section for ^{89}Zr varies between 3 and 25 mb.

We have estimated a maximum of 1.7% of ICF fraction contribution in ^{89}Zr at 71.7 MeV. Based upon the variation of ICF with entrance channel mass asymmetry and incident energy by Morgenstern *et al.* [29], small ICF for ^{12}C-induced reactions in the medium mass region [30] for energy below 7 MeV/nucleon is predicted. The same was also confirmed by reports on ^{12}C + ^{93}Nb, ^{89}Y collisions [10,11]. Several studies on ^{12}C-induced reactions in the energy range,
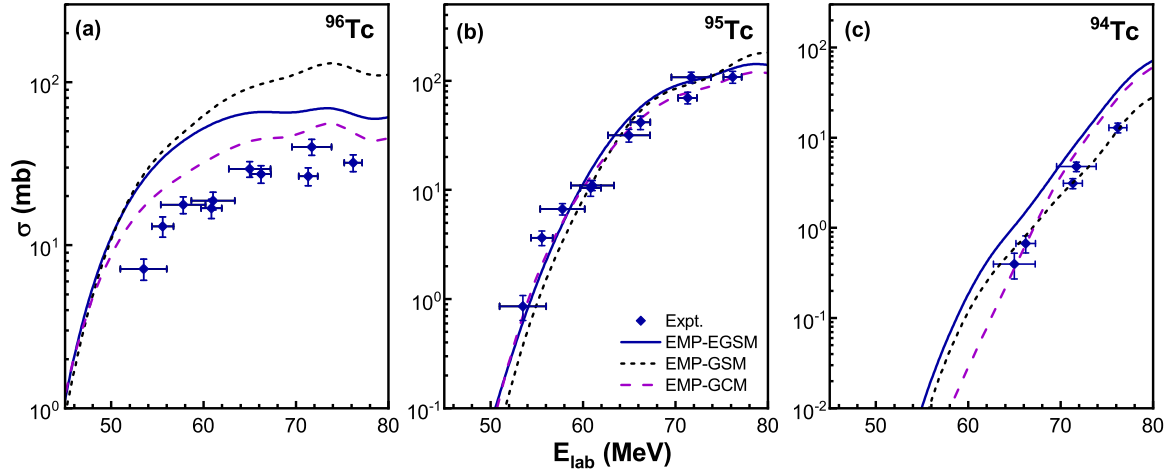
FIG. 8. Same as Fig. 3 for Tc residues obtained through the αpxn channel. The extracted independent cross sections for ^{95,94}Tc have been plotted.

< 7 MeV/nucleon, corroborate this theory [30] for a range of target masses: ^{103}Rh, ^{115}In, ^{128}Te, ^{159}Tb, and ^{165}Ho. ICF fraction varying between 2% and 10% has been reported for the ^{7}Li + ^{nat}Zr reaction [17] below 7 MeV/nucleon with respect to EMPIRE-3.2.2. An apparent effect of the projectile's weakly bound nature and higher mass asymmetry can be understood. We emphasize that more ICF processes can be observed for the ^{12}C + ^{nat}Zr reaction at higher energies, as the projectile breakup is more likely with the increase in energy. However, more studies in this mass region can better draw a conclusive argument about the appropriate theory/method to understand the reaction process.

From the detailed analysis of EFs of all the ERs, it can be seen that the EMPIRE-3.2.2 code working on HF and Exciton models under the framework of CF (details in Sec. III) has explained the data quite satisfactorily in most cases. Though

different level densities of EMPIRE justify the data in different cases, EGSM agrees remarkably with many of the trends for the maximum energy range compared to other level-density forms. Although the EFs of ^{98}Pd, ^{96}Tc, and ^{93m}Mo differ somewhat from theoretical estimations of the model code, the analysis seems to reach an overall understanding of the phenomenon.

We further made an effort to understand the effect of other modules of EMPIRE, such as multistep direct (MSD) and multistep compound (MSC), compared to the exciton model. However, the results of MSD and MSC were null for the present reaction, and no noticeable change in the ER cross section was observed. The hybrid Monte Carlo simulations (DDHMS) module incorporates only the emission of nucleons. As a result, the exciton model PCROSS turns out to be an optimum choice as its output comprises PEQ contributions due to light particle and cluster emissions. The contribution from direct/transfer reaction seems negligible, and the same has not been predicted by EMPIRE. The latter might be due to the lack of compatibility between the PEQ module PCROSS and the direct reaction module ECIS/OPTMAN incorporated by EMPIRE [40]. Nevertheless, a little ICF cross section and no positive Q value for nucleon transfer between the colliding partners suggest negligible interference of the direct reaction mechanism.

B. Total ER cross section ($\Sigma \sigma_{ER}$)

The total ER cross section ($\Sigma \sigma_{ER}$) measured from the sum of sixteen ERs' data was compared with EMPIRE-3.2.2 results (Fig. 10). It is essential to acknowledge that not all the ERs produced in the reaction were measured/identified due to their $T_{1/2}$. EMPIRE calculated $\Sigma \sigma_{ER}$ corresponding to the measured (m) ERs could precisely satisfy the experimental data within the experimental uncertainty. Though all the level densities of EMPIRE explain the measured data for the sum of ERs (not shown), EGSM was observed justifying the individual EFs for most of the ERs in the lower as well as higher energy regimes.

As the experimental $\Sigma \sigma_{ER}$ is justified by EMPIRE-3.2.2 model code, it seems fair to assume that it can adequately predict the rest of the unmeasured ERs. In this case, the data
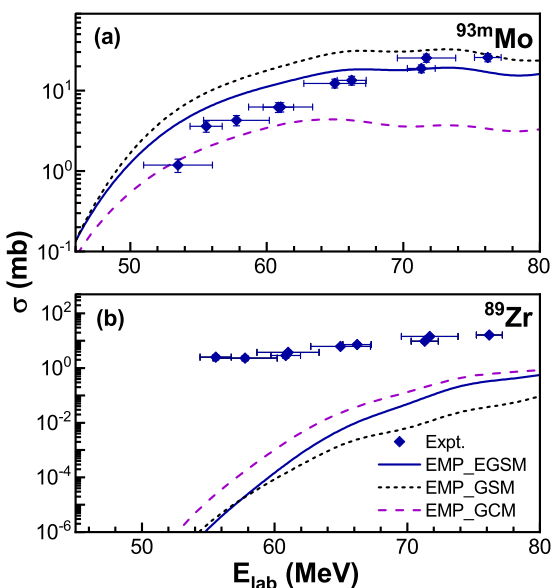

FIG. 9. Same as Fig. 3 for ^{93m}Mo and ^{89}Zr obtained through $2\alpha xn$ and $3\alpha xn$ channels, respectively.
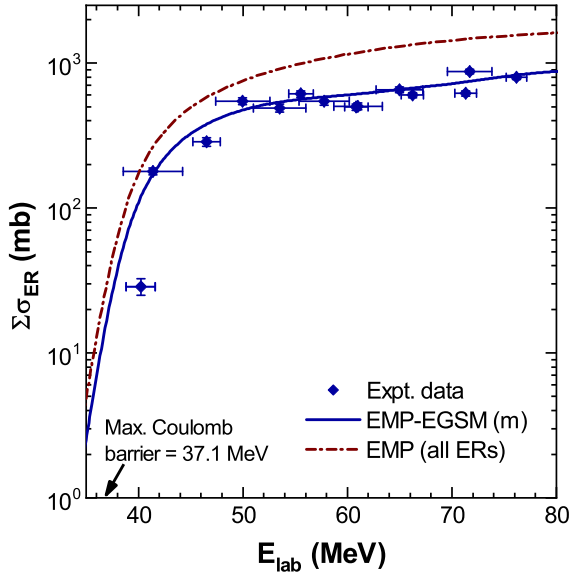
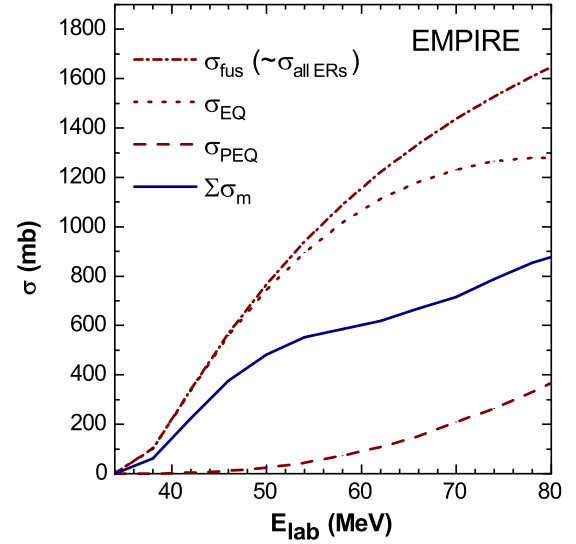FIG. 10. Comparison of experimental total evaporation residue (ER) cross section with that predicted by EMPIRE-3.2.2.

FIG. 11. Relative contribution of the preequilibrium (PEQ) and equilibrium (EQ) processes in ^{12}C + Zr based upon EMPIRE-3.2.2 predictions.

should fall upon the wine-colored dash-dotted line for the $\Sigma\sigma_{ER}$ of all the ERs (measured+unmeasured) predicted by the model code. For the highest energy, i.e., 76.2 MeV, the EMPIRE predicted $\Sigma\sigma_{ER}$ (all) is 1560 mb, while the experimentally measured value is only 798 ± 31 mb. The difference can be attributed to the unmeasured residues populated by the collision (Table V).

C. PEQ analysis

The EFs of ERs produced from the ^{12}C + Zr reaction were satisfactorily explained by EMPIRE-3.2.2. As the ^{nat}Zr target consists of five isotopes, visually disentangling the PEQ from EQ phenomena is challenging through the EF measurement (Fig. 4). However, one might achieve that through EMPIRE predicted total fusion cross section, i.e., $\sigma_{fus} = \sigma_{EQ} + \sigma_{PEQ}$. Further, $\sigma_{fus} \approx \sigma_{allERs}$, as the fusion-evaporation is a dominant phenomenon in this projectile-target mass range. σ_{allERs} comprise the measured as well as unmeasured ERs. Figure 11

TABLE V. List of major EMPIRE-EGSM predicted but unmeasured ERs during the experiment at 76.2 MeV

Unmeasured residue	Half-life $(T_{1/2})$	Cross section (mb)
^{102}Pd	Stable	21
^{102m}Rh	3.742 yr	26
^{98}Rh	8.72 min	129
^{100}Ru	Stable	30
^{99}Ru	Stable	67
^{98}Ru	Stable	139
^{96}Ru	Stable	68
^{97}Tc	4.21×10^{6} yr	32
^{92}Mo	Stable	29
^{90}Zr	Stable	20

represents EMPIRE predicted σ_{fus} at different energies and its segregation under the EQ and PEQ processes. The contribution from the EQ or compound nuclear process initially dominates (99%). However, it decreases to $\approx$79% at 78 MeV, while the PEQ process has little contribution in the lower energy range, i.e., $\approx$3% up to 50 MeV, that becomes $\approx$21% at 78 MeV. The EQ process constitutes the major contributor to most of the observed energy.

Also, the figure shows the EMPIRE-EGSM predicted $\Sigma\sigma_m$ for the experimentally measured (m) residues. The missing or unmeasured ER contribution is increasing significantly with energy. Nevertheless, observing the growing nature of $\Sigma\sigma_m$, similar to σ_{allERs}, an indirect inference about the increase of PEQ phenomenon with respect to incident energy can be drawn for the observed reaction process. Additionally, the model calculation does not explicitly estimate the contribution of EQ and PEQ phenomena for individual residues. However, evidence of the PEQ emission in ^{12}C-induced reactions in a similar mass region has been reported in the literature [5,7,10,11].

D. Nuclear potential parameters

One of the fundamental aspects of nuclear reactions is to know about the sensitive features of nuclear interaction, such as nuclear potential parameters, which include the depth of the potential and the barrier radius. Though there are several ways to extract these parameters, an indirect way is to obtain them from the experimental total fusion data using the Wong formulation [44]. For the present intermediate-mass system, the contribution of direct reactions is found to be negligible. Thus, the expression for the total fusion cross section (σ_{fus}) equals that of the reaction cross section (σ_r):

$$\sigma_{fus}(E_{c.m.}) = \pi \lambdabar^2 \sum_{\ell=0}^{\infty} (2\ell + 1) T_\ell(E_{c.m.}) \quad (5)$$
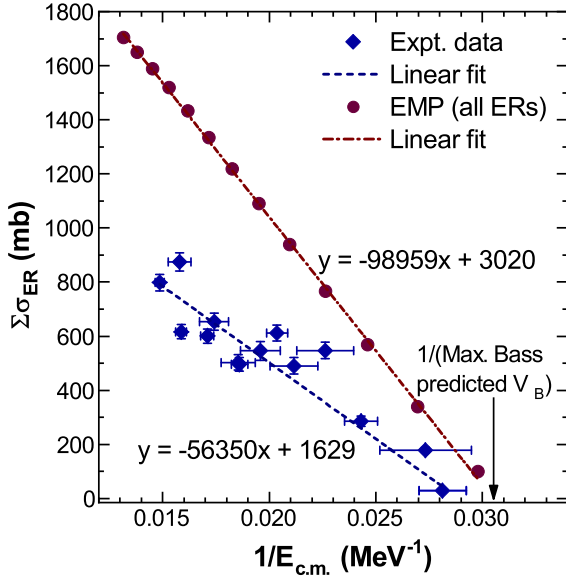
FIG. 12. Total evaporation residue (ER) cross section as a function of $1/E_{c.m.}$ to derive the nuclear potential parameters through the Wong formulation.

Here T_ℓ is the absorption probability of the ℓth partial wave for an incident energy $E_{c.m.}$. We can obtain $T_\ell(E_{c.m.})$ using Hill Wheeler approach [45]. Solving further, Wong finds that, for a diffuse well with the parameters of Viola and Sikkeland [46], s-wave parametrization is rather valid; hence, the interaction barrier becomes equal to the Coulomb barrier (V_B). For incident energies much above V_B, $E_{c.m.} - V_B \gg \hbar\omega_0/2\pi$, one obtains the simple analytical expression of σ_{fus},

$$\sigma_{fus}(E_{c.m.}) = \pi R_B^2 \left(1 - \frac{V_B}{E_{c.m.}} \right). \tag{6}$$

Equation (6) depicts the linear dependence of σ_{fus} on $1/E_{c.m.}$, through which the fusion barrier height and radius (V_B and R_B) can be extracted. It must be added that such linear dependence only holds for energies much higher than V_B and tends to diminish near V_B. Interestingly $\Sigma\sigma_{ER}$ should be $\approx \sigma_{fus}$ for the presently studied mass region as the fusion-evaporation is dominating (Fig. 11). The variation of $\Sigma\sigma_{ER}$ with $1/E_{c.m.}$ for the ^{12}C + ^{nat}Zr reaction is shown in Fig. 12. The EMPIRE predicted $\Sigma\sigma_{ER}$ for all the residues gives a more precise value

of the parameters near the range of Bass predicted values corresponding to different Zr isotopes (Table VI). Hence, the present experimental estimations of $\Sigma\sigma_{ER}$ are reliable, and the barrier parameters can be extracted by measuring the rest of the unidentified ERs (Table V) through some other experimental techniques.

V. CONCLUSION

We have reported a new study of ^{12}C + ^{nat}Zr reaction dynamics in the energy range 40.2–76.2 MeV (3.4–6.3 MeV/nucleon) using the activation technique. A total of 16 evaporation residues through xn, pxn, αxn, αpxn, $2\alpha xn$, and $3\alpha xn$ channels were identified and measured. The cross section data were compared with the theoretical model code EMPIRE-3.2.2 with EGSM, GSM, and GCM level densities. The model code based upon the Hauser-Feshbach formalism for the compound process and the exciton model for the precompound process showed a very sound prediction of the excitation functions. The EGSM level density was the most satisfactory choice, however; the excitation functions of ^{98}Pd, ^{96}Tc, and ^{93m}Mo could not be fully explained by the model code. Minute signatures of the incomplete fusion phenomenon were observed. The experimental total ER cross section complies well with the theoretical prediction, which led us to estimate the cross section of unmeasured ERs through the model code. An idea about the relative involvement (%) of both the compound and precompound processes in the reaction was formed. Nuclear potential parameters such as potential depth and range were extracted from the experimental data using the Wong formula. The difference with respect to Bass predicted values might be due to the unmeasured ERs. A conclusion about the excellent predictive ability of EMPIRE-3.2.2 model code can also be drawn.

TABLE VI. Nuclear potential parameters predicted by the Wong formula and Bass model for the ^{12}C + ^{nat}Zr reaction.

Method	Barrier height V_B (MeV) (in center-of-mass frame)	Barrier radius R_B (fm)
Wong formalism on experimentally measured $\Sigma\sigma_{ER}$	34.59 ± 0.17	7.20 ± 0.24
Wong formalism on EMPIRE predicted $\Sigma\sigma_{ER}$ (all)	32.76 ± 0.09	9.81 ± 0.02
Bass model	32.73 – 32.29	9.77 – 9.92

[1] J. Acharya, S. Mukherjee, G. F. Steyn, N. L. Singh, and A. Chatterjee, Phys. Rev. C **93**, 024608 (2016).

[2] J. Gómez del Campo, D. Shapira, J. McConnell, C. J. Gross, D. W. Stracener, H. Madani, E. Chávez, and M. E. Ortíz, Phys. Rev. C **60**, 021601(R) (1999).

[3] M. P. Kelly, J. F. Liang, A. A. Sonzogni, K. A. Snover, J. P. S. van Schagen, and J. P. Lestone, Phys. Rev. C **56**, 3201 (1997).

[4] V. L. Kravchuk, S. Barlini, and O. V. Fotina, EPJ Web Conf. **2**, 10006 (2010).

[5] C. Birattari, M. Bonardi, M. Cavinato, E. Fabrici, E. Gadioli, E. Gadioli Erba, F. Groppi, M. Bello, C. Bovati, A. Di Filippo *et al.*, Phys. Rev. C **54**, 3051 (1996).

[6] M. Cavinato, E. Fabrici, E. Gadioli, E. Gadioli Erba, P. Vergani, M. Crippa, G. Colombo, I. Redaelli, and M. Ripamonti, Phys. Rev. C **52**, 2577 (1995).

[7] M. K. Sharma, P. P. Singh, D. P. Singh, A. Yadav, V. R. Sharma, I. Bala, R. Kumar, Unnati, B. P. Singh, and R. Prasad, Phys. Rev. C **91**, 014603 (2015).

[8] F. Amorini, M. Cabibbo, G. Cardella, A. Di Pietro, P. Figuera, A. Musumarra, M. Papa, G. Pappalardo, F. Rizzo, and S. Tudisco, Phys. Rev. C **58**, 987 (1998).

[9] P. Vergani, E. Gadioli, E. Vaciago, E. Fabrici, E. Gadioli Erba, M. Galmarini, G. Ciavola, and C. Marchetta, Phys. Rev. C **48**, 1815 (1993).

[10] M. Sagwal, M. Maiti, T. N. Nag, and S. Sodaye, Eur. Phys. J. Plus **136**, 1057 (2021).

[11] A. Chauhan, M. Maiti, and S. Lahiri, Phys. Rev. C **99**, 064609 (2019).

[12] R. Kumar, M. Maiti, G. Sarkar, M. Sagwal, P. Kaur, R. Prajapat, T. N. Nag, and S. Sodaye, Eur. Phys. J. A **57**, 209 (2021).

[13] R. Kumar, M. Maiti, T. N. Nag, and S. Sodaye, Phys. Rev. C **104**, 064606 (2021).

[14] D. Kumar and M. Maiti, Phys. Rev. C **95**, 064602 (2017).

[15] R. Prajapat and M. Maiti, Phys. Rev. C **103**, 034620 (2021).

[16] R. Prajapat and M. Maiti, Phys. Rev. C **101**, 064620 (2020).

[17] R. Prajapat and M. Maiti, Phys. Rev. C **101**, 024608 (2020).

[18] D. Kumar, M. Maiti, and S. Lahiri, Phys. Rev. C **96**, 014617 (2017).

[19] D. Kumar and M. Maiti, Phys. Rev. C **96**, 044624 (2017).

[20] D. Kumar, M. Maiti, and S. Lahiri, Phys. Rev. C **94**, 044603 (2016).

[21] R. Kumar, R. Prajapat, and M. Maiti, J. Phys. G: Nucl. Part. Phys. **50**, 025106 (2023).

[22] W. Hauser and H. Feshbach, Phys. Rev. **87**, 366 (1952).

[23] J. J. Griffin, Phys. Rev. Lett. **17**, 478 (1966).

[24] P. Kaur and M. Maiti, Eur. Phys. J. Plus **137**, 1287 (2022).

[25] A. Singh, M. Maiti, T. N. Nag, and S. Sodaye, Phys. Scr. **98**, 025306 (2023).

[26] L. F. Canto, P. R. S. Gomes, R. Donangelo, J. Lubian, and M. S. Hussein, Phys. Rep. **596**, 1 (2015).

[27] V. Jha, V. V. Parkar, and S. Kailas, Phys. Rep. **845**, 1 (2020).

[28] P. K. Rath, S. Santra, N. L. Singh, R. Tripathi, V. V. Parkar, B. K. Nayak, K. Mahata, R. Palit, S. Kumar, S. Mukherjee *et al.*, Phys. Rev. C **79**, 051601(R) (2009).

[29] H. Morgenstern, W. Bohne, W. Galster, K. Grabisch, and A. Kyanowski, Phys. Rev. Lett. **52**, 1104 (1984).

[30] A. Yadav, V. R. Sharma, P. P. Singh, D. P. Singh, M. K. Sharma, U. Gupta, R. Kumar, B. P. Singh, R. Prasad, and R. K. Bhowmik, Phys. Rev. C **85**, 034614 (2012).

[31] B. B. Kumar, A. Sharma, S. Mukherjee, S. Chakrabarty, P. K. Pujari, B. S. Tomar, A. Goswami, S. B. Manohar, and S. K. Datta, Phys. Rev. C **59**, 2923 (1999).

[32] S. Mukherjee, A. Sharma, S. Sodaye, A. Goswami, and B. S. Tomar, Int. J. Mod. Phys. E **15**, 237 (2006).

[33] M. K. Sharma, B. P. Singh, S. Gupta, M. Musthafa, H. D. Bhardwaj, R. Prasad, and A. K. Sinha, J. Phys. Soc. Jpn. **72**, 1917 (2003).

[34] S. Gupta, B. P. Singh, M. M. Musthafa, H. D. Bhardwaj, and R. Prasad, Phys. Rev. C **61**, 064613 (2000).

[35] P. Kaur, M. Maiti, T. N. Nag, and S. Sodaye, Phys. Rev. C **105**, 014629 (2022).

[36] J. F. Ziegler, M. D. Ziegler, and J. P. Biersack, Nucl. Instrum. Methods Phys. Res., Sect. B **268**, 1818 (2010).

[37] M. Maiti and S. Lahiri, Phys. Rev. C **81**, 024603 (2010).

[38] http://www.nndc.bnl.gov/nudat3/.

[39] http://nucleardata.nuclear.lu.se/toi/.

[40] M. Herman, R. Capote, B. V. Carlson, P. Obložinský, M. Sin, A. Trkov, H. Weinke, and V. Zerkin, Nucl. Data Sheets **108**, 2655 (2007).

[41] C. Kalbach, Z. Physik A **283**, 401 (1977).

[42] A. Iwamoto and K. Harada, Phys. Rev. C **26**, 1821 (1982).

[43] R. Capote, M. Herman, P. Obložinský, P. G. Young, S. Goriely, T. Belgya, A. V. Ignatyuk, A. J. Koning, S. Hilaire, V. A. Plujko *et al.*, Nucl. Data Sheets **110**, 3107 (2009).

[44] C. Y. Wong, Phys. Rev. Lett. **31**, 766 (1973).

[45] D. Hill and J. Wheeler, Phys. Rev. **89**, 1102 (1953).

[46] V. E. Viola and T. Sikkeland, Phys. Rev. **128**, 767 (1962).